energy&fuels

pubs.acs.org/EF Article

Determination of Flame Temperatures and Soot Volume Fractions during Combustion of Biomass Pellets

Weijie Yan,* Kuangyu Li, Tianze Yu, Xianliang Huang, Lingbo Yu, Aidin Panahi, and Yiannis A. Levendis*

Cite This: *Energy Fuels* 2021, 35, 2313−2325 Read Online

ACCESS | Metrics & More | Article Recommendations

ABSTRACT: This article presents a method for real-time simultaneous measurements of the temperature and soot volume fraction distribution of volatile matter flames, forming during combustion of biomass pellets. This method uses flame radiation spectra, captured by a spectrometer, and images, captured by a digital camera, as inputs during combustion of three different types of biomass pellets (pine wood, rice straw, and corn straw). The pellets were ignited and burned in the post-combustion zone of methane gas at 1300 K. The radiation spectrum of the flame in the 500−800 nm wavelength band was selected for spectral analysis, combined with a spectral emissivity model based on polynomial fitting. The flame emissivity was measured at the response wavelengths of a dual band-pass filter (centered at 615 and 517 nm) fitted on the camera, and the resulting emissivity ratio showed the degree of departure from the gray radiation model. The measured emissivity ratio approached unity as the combustion intensity increased. The emissivity ratio of the spectrometer measurement was used to correct the flame temperature measurement obtained by the image method. Upon correction, the maximum relative error of the image temperature measurement was determined to be 2.7% by comparison to thermocouple readings. The experimental results showed that the maximum flame temperatures of pine wood, rice straw, and corn straw pellets were remarkably similar at 1876 ± 2 K. Moreover, the flame burnout durations and the peak soot volume fractions were both positively correlated with the volatile content of biomass pellets; the value of the latter was 1.19 ± 3 ppm. The experimental results measured in this article can provide data for models of the soot generation mechanism of biomass pellet combustion in industrial furnaces.

1. INTRODUCTION

Renewable biomass is a green energy source. Compared with coal and other fossil fuels, biomass combustion generates lower SO*x* and, in some cases, lower NO*x* emissions and can achieve near-zero net CO_2 emissions. As a result, it has broad application prospects.[1] Biomass fuels release volatile matter during their pyrolysis. The volatiles generate soot during their combustion process. The generation of soot affects the radiative heat transfer in furnaces, and emissions of unburned soot pollute the environment.[2] The main components of the volatile matter produced by biomass pyrolysis are high-molecular-weight hydrocarbons (tars).[3,4] Hence, compared with simple hydrocarbon fuels, such as natural gas, the mechanism of soot generation during biomass combustion is more complicated.[5−8] Experimental research is important in the development of the soot generation mechanism during the combustion of biomass which, in turn, can be of great significance for improving the efficiency of combustion.

The physical morphology[9−12] and chemical composition[9,13−17] of the soot in different combustion zones can be obtained by sampling the soot in flames generated during biomass combustion, combined with off-line analysis (such as SEM/EDS, XRD, and FTIR). Trubetskaya et al.[10] studied the particle size distribution of soot generated during the combustion of pine wood, beech wood, and wet straw through sampling techniques. Their results showed that the particle size distribution of soot generated during pine wood combustion, in air at a temperature of 1250 °C, was the widest (27.2−263 nm), and the particle size distribution of soot generated in beech wood was the narrowest (33.2−102 nm). They partly attributed such differences to the different potassium contents of fuels. Wiinikka et al.[13] reported that combustion of wood chips generated soot particles with two different modes, the fine mode and coarse mode. In an oxygen-rich combustion zone (at ∼1000 °C), the mass concentration of soot particles was reduced. Li et al.[12] reported that the main component of $PM_{2.5}$ particles produced during wet straw pyrolysis at temperatures in the range of 900−1000 °C was char-carbon, while the major component in particles during pyrolysis at higher temperatures (1000−1100 °C) was soot.

In recent years, real-time combustion diagnosis technology has been widely used in the experimental study of soot generation during biomass combustion. The aerosol time-of-flight mass spectrometry (ATOFMS) technology[18−20] and

Received: November 21, 2020
Revised: December 24, 2020
Published: January 13, 2021

https://dx.doi.org/10.1021/acs.energyfuels.0c03921
Energy Fuels 2021, 35, 2313−2325

molecular-beam mass spectrometry technology[21] have been used to measure the detailed molecular composition of soot. Laser diagnostic techniques such as LII,[22−24] LEM,[25−27] and TDLAS[28−30] have been used to measure the soot generation concentration during biomass burning. Gao et al.[23] burned methyl decanoate (MD) and added dibutyl ether (DBE), a wood biomass extract; they studied the effects of this additive on the generation of soot. They measured the soot concentration distribution using the two-dimensional LII technology. They found out that the addition of DBE reduced the PAH concentration and the nucleation rate of soot along the flame axis, thereby suppressing the concentration of soot. Göktepe et al.[26] used the LEM technology to study the influence of particle dispersion characteristics on the concentration of soot generated during the combustion of pine wood chips. Their experimental results showed that the increase in the wood particle dispersion distance reduced the soot concentration peak (by 35−56%) but did not affect the location of the soot concentration peak. Sepman et al.[28] used the TDLAS technology to measure in various real-time parameters, such as soot volume fraction, temperature, water vapor concentration, and potassium concentration, during biomass combustion. The measurement device of that technology is relatively complex. Their results showed that the soot volume fraction decreases with the increasing equivalence ratio (in the range of φ = 0.35−1.2) during the combustion of stem wood and peat. Under the equivalence ratio of φ = 0.5, the soot volume fraction generated by the combustion of stem (mixed by pine and spruce) wood (f_v = 1.0 ppm) was higher than that of peat (f_v = 0.6 ppm). The difference in volatile content was given as the main reason for the different volume fraction of soot produced by the combustion of these two biomass samples. Sepman et al.[29] have recently conducted an experimental study on the oxyfuel combustion of biomass using the TDLAS technology. They showed that oxyfuel combustion (at 30 and 40% O_2) can reduce the soot generation of biomass fuels, as compared to combustion in air. The aforementioned laser diagnosis technologies (LII, LEM, and TDLAS) have the advantage of high measurement accuracy, but the measurement devices and operability are relatively complicated and cannot easily accomplish the simultaneous measurement of the soot concentration and flame temperature.

Based on the radiation image or spectrum, the temperature and soot concentration of a flame can be measured simultaneously in real time. However, the measurement process usually needs either to assume that the combustion flame behaves as a graybody in a given wavelength band[24,26,30,31] or to use an existing emissivity model in the literature.[31−33] Levendis and co-workers[33,34] used a three-wavelength pyrometer to measure the combustion temperature of single sugarcane bagasse and coal particles. A linear emissivity function with a wavelength was used in the temperature measurement. The gas (air) temperature in the furnace was 1350 K, and the maximum temperature of bagasse chars was determined to be in the neighborhood of 1900 K. Jing et al.[32] measured the temperature field and KL factor distribution during the combustion of the BTL (biomass to liquid) fuel using a high-speed camera equipped with a dual band-pass filter (550 and 650 nm). Their results, based on the Hottel and Broughton's emissivity model, showed that the soot concentration decreased with the decrease of the ambient temperature. During combustion in air, at 800, 1000, and 1200 K, the corresponding BTL combustion temperature was, respectively, approximately 2300, 2400, and 2500 K. Toth et al.[30] used a two-color pyrometer to measure the temperature field of the flame, which resulted from burning oil derived from the fast pyrolysis of biomass. The operating wavelengths of their pyrometer were centered at 500 and 600 nm. They assumed the flame to emit as a graybody at those wavelengths; the temperature measured by the two-color pyrometer was higher than that measured by tunable diode laser absorption spectroscopy (TDLAS). The graybody assumption may be a reason for the higher-temperature value of the two-color method. These results illustrate that the accuracy of the emissivity model selection affects the accuracy of the temperature measurement.[35,36]

Based on the flame radiation spectrum, the temperature and spectral emissivity of the flame can be measured simultaneously.[37−42] The previous research by the authors[38] showed that the spectral emissivity of the flame of biomass pellets is a variable parameter during the combustion process and that directly adopting the graybody assumption or using the Hottel and Broughton's emissivity model can cause a temperature measurement error. In the wavelength band of 400−700 nm, the average emissivity of biomass volatile flames was determined to be 0.16 at an equivalence ratio of φ = 0.91, whereas it was 0.10 at an equivalence ratio of φ = 0.71. Results from the related research[37] showed that the spectral emissivity of the flame of biomass volatiles depends on the type of biomass. The emissivity of the flame of rice husk volatiles in the 400−900 nm band is lower than that of the pine wood. Hence, if the radiation spectrum and radiation image of an object can be measured simultaneously in the same wavelength band, then the spectral emissivity of the object can be determined based on its radiation spectrum. Subsequently, the measured spectral emissivity can be used for correcting the temperature of the image method.[38,42,43] This improves the accuracy of the temperature measurement. In a previous study, the accuracy of this method was verified by using R-type platinum−rhodium filament thermocouples.[43] By comparison to the thermocouple temperature reading, the maximum relative error of the image temperature measurement was 0.62% under steady-state conditions, while the maximum relative error was 0.75% under nonsteady-state conditions. It appears that this method has high measurement accuracy.

This article describes an experimental study on the volatile matter flame of a biomass pellet, where a spectrometer and a color camera were used to simultaneously collect the two-dimensional radiation spectrum and image of the flame, respectively, during the combustion process. The collected radiation spectrum was used to calculate the spectral emissivity of the flame during the entire duration of its combustion from ignition to burnout. Real-time measurements of spectral emissivity were subsequently used to calculate the ratio of emissivity. This, in turn, was used in the temperature measurement of the flame, by the image method, and the determination of its soot volume fraction. These parameters are very important in the operation of utility furnaces, as they affect the radiation fluxes to the water tubes. Three types of biomass, pine wood, rice straw, and corn stalk, were burned in these experiments, and the two-dimensional distributions of the temperature and soot volume fraction in

https://dx.doi.org/10.1021/acs.energyfuels.0c03921
Energy Fuels 2021, 35, 2313−2325

their volatile matter flames were measured as a function of time at different degrees of burnout. In the previous research,[38] the size and disturbance of a biomass semi-gasification flame were found to be relatively large, and thus, the flame absorption path length required to calculate the soot concentration could not be accurately obtained. Therefore, no measurement results of soot concentration distribution were given in the previous research. Compared with the semi-gasification flame in the previous research, the pellet combustion flame sizes in this study were very small, and the flames had almost no disturbance; thus, the flame absorption path length could be accurately measured and the soot concentration distribution could be calculated.

2. MEASUREMENT PRINCIPLE

2.1. Principle of Spectral Thermometry Based on the Nongray Emissivity Model. According to Planck's law, the spectral radiation intensity of a flame at temperature T can be expressed as

$$I(\lambda, T) = \varepsilon(\lambda)\cdot\frac{2\pi hc^2}{\lambda^5(e^{hc/\lambda kT} - 1)} \tag{1}$$

In eq 1, $I(\lambda,T)$ is the spectral radiant intensity, W/m^3; $\varepsilon(\lambda)$ is the spectral emissivity; h is the Planck constant, J·s; c is the speed of light, m/s; k is the Boltzmann constant, J/K; and λ is the wavelength, m. Using a color camera that is equipped with a dual narrow band-pass filter, two monochrome flame images at different wavelengths can be obtained simultaneously.[44] Then the image intensities of the two different wavelengths of the electronic color camera can be expressed as

$$S_i = \eta_i\cdot I(\lambda_i, T)\cdot\tau = \eta_i\cdot\varepsilon(\lambda_i)\cdot\frac{2\pi hc^2}{\lambda_i^5(e^{hc/\lambda_i kT} - 1)}\cdot\tau \qquad i = 1,2 \tag{2}$$

In eq 2, S_i is the intensity of the monochromatic image at a given wavelength λ_i; η_i is the relative spectral response efficiency of the system, including the spectral response characteristics of the camera lens, the sensor CFA (color filter array), and the dual narrow band-pass filter at the wavelength λ_i; and τ is the exposure time of the camera in seconds. Then, the ratio of the intensities of the monochrome images at two different wavelengths can be expressed as

$$\frac{S_1}{S_2} = \frac{\eta_1\cdot\varepsilon(\lambda_1)\cdot\frac{2\pi hc^2}{\lambda_1^5(e^{hc/\lambda_1 kT} - 1)}}{\eta_2\cdot\varepsilon(\lambda_2)\cdot\frac{2\pi hc^2}{\lambda_2^5(e^{hc/\lambda_2 kT} - 1)}} \tag{3}$$

In eq 3, η_1/η_2 is an unknown parameter, which can be obtained by the calibration of the camera with a standard radiation source of known emissivity. In this study, a blackbody furnace was used for calibration; in this case, $\varepsilon(\lambda_1) = \varepsilon(\lambda_2) = 1$. For the blackbody, the correspondence between S_1/S_2 and temperatures was readily established. However, when measuring the flame, the ratio $\varepsilon(\lambda_1)/\varepsilon(\lambda_2)$ is an unknown parameter, and hence, it needs to be determined. For this purpose, the multispectral algorithm presented in a previous paper was used to measure the spectral emissivity $\varepsilon(\lambda)$ of the soot flame in real time.[38,43] The spectral emissivity of the flame can be expressed by a polynomial function

$$\varepsilon(\lambda_j) = a_0 + a_1\cdot\lambda_j + a_2\cdot\lambda_j^2 + \ldots + a_m\cdot\lambda_j^m, \qquad j = 1,2,3, \ldots, n \tag{4}$$

where m is the series of polynomial; a_m is the polynomial coefficient; j is any of the number of measured effective wavelengths within the spectral response range of the spectrometer; and n is the number of measuring wavelengths of the spectrometer. Substitution of eqs 4 into 1 gives

$$I(\lambda_j, T) = (a_0 + a_1\cdot\lambda_j + a_2\cdot\lambda_j^2 + \ldots + a_m\cdot\lambda_j^m)\cdot\frac{2\pi hc^2}{\lambda_j^5(e^{hc/\lambda_j kT} - 1)}, \qquad j = 1,2,3, \ldots, n \tag{5}$$

There is a minimum value in eq 5, which can be obtained numerically by the Newton iteration method

$$|f|^2 = \sum_{j=1}^{n}\left[I(\lambda_j) - (a_0 + a_1\cdot\lambda_j + a_2\cdot\lambda_j^2 + \ldots + a_m\cdot\lambda_j^m)\cdot\frac{2\pi hc^2}{\lambda_j^5(e^{hc/\lambda_j kT} - 1)}\right]^2 \qquad j = 1,2,3, \ldots, n \tag{6}$$

As a result, $\varepsilon(\lambda_j)$ can be calculated, and the ratio $\varepsilon(\lambda_1)/\varepsilon(\lambda_2)$ is obtained. The $\varepsilon(\lambda_1)/\varepsilon(\lambda_2)$ ratio is used for correcting the correspondence between temperature and the ratio of S_1/S_2. The flames of the volatile matter of biomass pellets are sooty. After the soot temperature is measured, the soot volume fraction can be calculated according to eq 7[45,46]

$$f_v = -\frac{\lambda_S}{K_{ext}L}\ln\left\{1 - \frac{\sigma_S}{\sigma_B}\cdot\frac{S_{S\lambda}}{S_{B\lambda}}\cdot\exp\left[-\frac{hc}{k\lambda_S}\left(\frac{1}{T_B} - \frac{1}{T_S}\right)\right]\right\} \tag{7}$$

In eq 7, the subscripts S and B represent the soot and blackbody furnace, respectively; λ_S is the measurement wavelength; K_{ext} is the dimensionless extinction coefficient, which was selected as 8.6 in this article;[47] L is the absorption path length (the absorption path L at any pixel in the flame image can be obtained based on the flame radius at the height of the pixel and the distance between the pixel and the flame axis); σ_S and σ_B are optical parameters for the measurement of flame and the blackbody furnace calibration, respectively. It should be noted that the flame temperature and soot concentration measured in this article are the average values in the line of sight.

3. EXPERIMENTAL SETUP

3.1. Biomass Selection, Analysis, Pulverization, and Palletization. In this article, three different raw biomass materials have been selected from Jiangsu Province, China, which are pine wood, rice straw, and corn stalk. The proximate and ultimate analysis of the three raw biomass materials is shown in Table 1. The volatile content of pine wood is the highest, followed by that of rice straw and then by that of corn stalk. The ash content of rice straw is the highest, followed by that of corn stalk and then by that of pine wood, a distant third. Ultimate analysis results show that the N content of pine wood is much lower than those of the other two biomass fuels; however, its S content is the highest. The amounts of H, O, and N are the highest in rice straw, but C is the lowest. The amount of C in corn stalk is the highest, while the contents of the elements H, O, and S are the lowest.

https://dx.doi.org/10.1021/acs.energyfuels.0c03921
Energy Fuels 2021, 35, 2313−2325

Table 1. Proximate Analysis and Ultimate Analysis of Raw Biomass Materials

parameter	pine wood	rice straw	corn stalk
Proximate Analysis (wt %, Air Dry Basis)			
fixed carbon	12.91	13.92	13.77
volatile matter	79.10	69.01	68.48
ash	0.36	10.86	9.21
moisture	7.63	6.21	8.54
Ultimate Analysis (wt %, Dry Ash Free)			
C	48.96	47.51	50.36
H	6.04	6.31	4.58
O	44.24	44.48	44.03
N	0.02	1.39	0.82
S	0.74	0.31	0.21

The biomass pellets used in the experiment were prepared by air drying, grinding, sieving, drying, and pressing. After sieving, biomass particles were selected in the size cut of 74−88 μm, which were collected between 180 and 200 mesh sieves. The drying temperature was 105 °C, the atmosphere was air, and the duration was 2 h. Upon drying, the biomass powder was pelletized by compression to cylindrical pellets with a diameter of 4 mm (±0.2 mm), a height of 3.5 mm (±0.2 mm), and a mass of 50 mg (±5 mg), as shown in Figure 1. A B-type platinum−rhodium filament thermocouple was

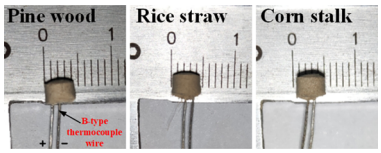

Figure 1. Biomass pellets.

embedded inside each pellet, both to provide support during the combustion and to measure the internal temperature of the pellets in real time. The diameter of the positive and negative thermocouple filaments of the B-type platinum−rhodium thermocouple was 0.3 mm, whereas the diameter of the junction was 0.5 mm. The process of embedding thermocouples into the biomass pellets has been described in the recent research.[48]

3.2. Biomass-Compressed Pellet Combustion Experimental Setup. The schematic of the experimental apparatus is shown in Figure 2. A Bunsen premixed burner was used to burn methane gas.[43] The flow of methane (CH_4) was set to 0.40 L/min, the flow of air was set to 4.85 L/min, and the resulting equivalence ratio was φ = 0.786. The B-type platinum−rhodium filament thermocouple wire inside the biomass pellets was supported by the thin corundum

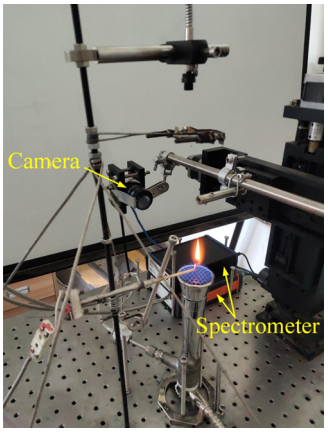

Figure 2. Schematic of the experimental apparatus.

tube and was fixed 20 mm above the burner. At this height, the temperature of the hot postflame gas was 1300 K (±20 K), as measured by another B-type platinum−rhodium thermocouple, in the absence of the biomass pellet burning. The air flow speed was 0.2 m/s. The platinum−rhodium thermocouple was connected to the data acquisition card through a cable. The data acquisition card collected the temperature values online, and the sampling frequency of the data acquisition card was 50 Hz. An **Avaspec-ULS2048-USB2** spectrometer was used to collect the radiation spectrum of the biomass volatile matter flame in real time. The spectral resolution of the spectrometer is 1.1 nm, and the spectral response range is 200−1100 nm. The optical fiber at the front end of the spectrometer is equipped with a collimating lens, so as to ensure that the flame of biomass pellets can be aligned. The collimating lens collected the radiation spectrum of the flame from the top of the pellet through the quartz glass, which played a role of protecting the collimating lens. In the process of data acquisition, the integration time of the spectrometer was set as 100 ms, and the sampling frequency was 10 Hz. A **MER-030-120 GC** color camera was used to record flame images during the combustion process of pellets.[38] The image resolution of the camera is 656 × 492, and the sensor model is **Sony ICX618 CCD**. The camera lens model is **Computar M1214-MP2**. The horizontal field of the view angle of the camera is 32°, and the vertical field of the view angle is 42°. The output image format of the camera is TIF with a 10-bit depth. The sampling frequency of the camera was set to 50 Hz. The front end of the camera lens was equipped with a dual narrow band-pass filter.[44] The two wavelengths of the band-pass filter were centered at 517 and 615 nm, respectively, and their full width at half-maximum was 10 nm. The use of the dual narrow band-pass filter can improve the monochromaticity of the image collected by the camera and avoid the interference of the characteristic spectra of potassium (K) (766.0 and 770.1 nm) and sodium (Na) (589.0 nm) alkali metals. The spectral response characteristics of the camera and the dual narrow band-pass filter are shown in Figure 3.

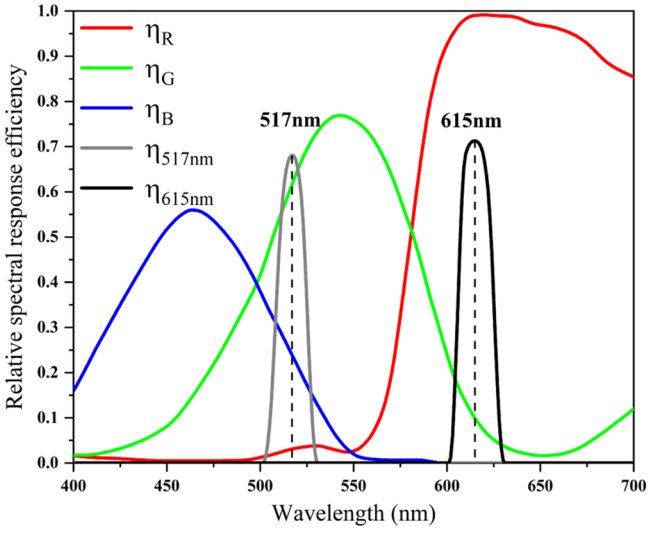

Figure 3. Relative spectral response curves of the R, G, and B bands of the camera and the dual narrow band-pass filter.

4. EXPERIMENTAL RESULTS AND DISCUSSION

Time-resolved flame images of the three compressed biomass pellets from the ignition of the volatile matter to its burnout are shown in Figure 4. In these photographs, the volatile matter flames of the biomass pellets appear to be red instead of the common yellow color. This coloration is caused by the dual band-pass filter installed in front of the camera. As the combustion process progressed, both the flame height and diameter increased, reached a maximum, and

https://dx.doi.org/10.1021/acs.energyfuels.0c03921
Energy Fuels 2021, 35, 2313−2325

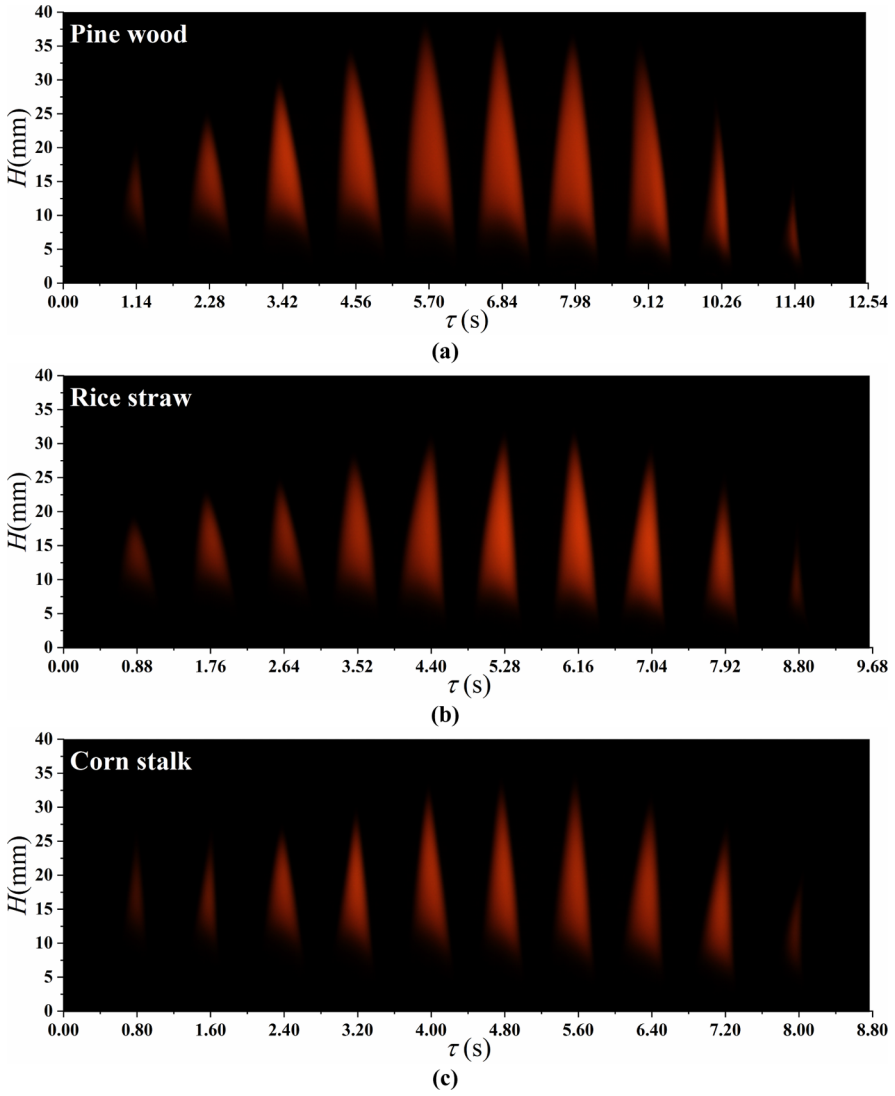

Figure 4. Images of time-resolved volatile flames of biomass pellets from (a) pine wood; (b) rice straw; and (c) corn stalk throughout the volatile matter burnout.

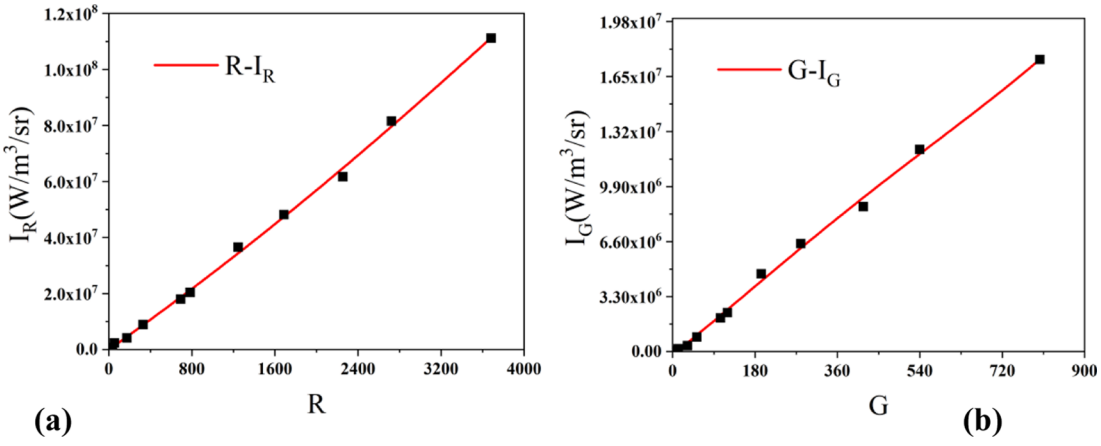

Figure 5. Blackbody calibration curves of the camera at the wavelengths of (a) 615 nm and (b) 517 nm.

then decreased. This trend is related to the time-dependent rate of the volatile release during the pyrolysis of biomass pellets. In addition, among the three types of biomass, the tallest flame belonged to pine wood, while the flame heights of rice straw and corn stalk were both similarly shorter. It can also be observed in Table 1 that the volatile content of pine wood is 79.1% and those of rice straw and corn stalk is 69.01 and 68.48%, respectively. The volatile content is one of the most important factors that affect the flame height. The amount of volatile content also affects the duration of the volatile flame. Accordingly, the respective durations

https://dx.doi.org/10.1021/acs.energyfuels.0c03921
Energy Fuels 2021, 35, 2313−2325

of the flames of the compressed biomass pellets of pine wood, rice straw, and corn stalk were 12.54, 9.68, and 8.80 s, respectively.

The flame image was recorded by the electronic color camera through the dual band-pass filter. The relative intensity from recorded images was then converted into radiation intensities. In this investigation, the color camera equipped with the dual band-pass filter was calibrated using the blackbody furnace, as described in the previous research.[44] The calibration coefficients are shown in Figure 5.

Using the calibration coefficients, based on the data shown in Figure 5, the volatile matter flame intensity images of Figure 4 were converted into radiation intensity images. The resulting radiation intensity images (through both the 517 and 615 nm bands of the filter) of the three types of biomass flames are shown in Figure 6. It can be noticed that the radiation intensities of the three different biomass flames, which are mostly contributed by soot particles, are lower at the 517 nm wavelength as compared to those at 615 nm. However, since the radiation intensity distributions corresponding to the two wavelengths are rather similar, only the radiation intensity distributions at the wavelength of 615 nm are analyzed below. For those three biomass volatile matter flames, the peak flame intensity (designated with red color in the cloud map) appeared in the center of the flame, and the time frames of the occurrence were as follows: for pine wood 3.42−9.12 s, for rice straw 5.28−7.04 s, and for corn stalk 4.00−6.40 s. The high radiant intensity of the pine wood-burning flame lasted for the longest (5.7 s) time and those of the corn stalk and rice straw were similar at 2.4 and 1.76 s, respectively. Such differences in the duration of the radiant intensities are attributed to the volatile contents of the three types of biomass.

The radiation spectrum distributions of the three types of biomass volatile matter flames, as measured by the spectrometer, are shown in Figure 7. In the 500−800 nm wavelength band, the radiation spectrum of the flame contains both the continuous spectrum and characteristic spectrum. The continuous spectrum is mainly generated by the thermal radiation of soot particles in the flame. Pyrolysis of biomass pellets releases volatile matter, and therefrom soot is generated in the flame.[49] The radiation intensity of the continuous spectrum increases with the increase of the wavelength, and the radiant intensity of the continuous spectrum is related to both the concentration of soot and its temperature.[35] The continuous spectrum is used for the multispectral temperature measurement.[38,50,51] During the combustion of volatile matter from the three types of biomass pellets, from ignition to burnout, the spectral radiation intensity of the generated flames showed a trend of first increasing and then decreasing. Comparing the peak radiation intensity of the continuous spectrum, the pine wood pellets have the strongest radiation intensity. In the 500−800 nm band, there are also three clear characteristic lines, namely, the 589.0 nm Na characteristic line and the 766.0 and 770.1 nm K characteristic lines.[52] This indicates that all three raw biomass materials are rich in Na and K alkali metals. The appearance of characteristic lines is accompanied by the entire combustion process of volatiles. Related studies have shown that the radiation intensity of the characteristic lines of Na and K is related to the concentration of Na and K in the flame.[53]

The existence of the discontinuous spectrum can cause an interference to the temperature measurement by the multispectral method.[35] Therefore, in this study, the characteristic lines of Na (589.0 nm) and K (766.0 and 770.1 nm) were first removed and, subsequently, the 500−800 nm wavelength range was selected as the temperature measurement interval. Using the emissivity model based on the polynomial fitting proposed in previous studies,[38,43] the emissivity ratio at the response wavelength of the camera color filters (517 and 615 nm) was calculated. This ratio was used in eq 3 to correct the corresponding relationship between the intensity of the monochromatic flame images, recorded by the camera, and the flame temperature and thus improve the accuracy of the two-dimensional temperature measurement. The calculated emissivity ratios for the three biomass types are shown in Figure 8 as a function of the volatile matter burnout times. It can be seen therein

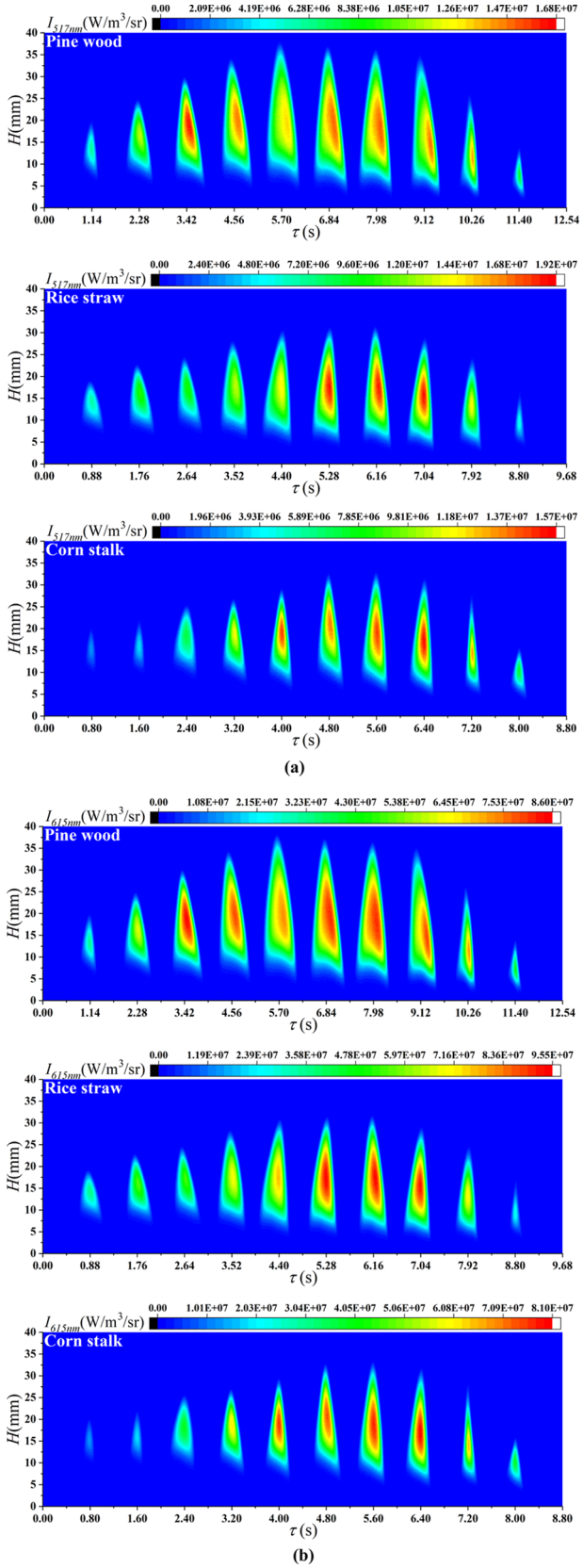

Figure 6. Flame radiation intensity images of three types of biomass pine wood, rice straw, and corn stalk flames through the bands of the filter centered at (a) 517 nm and (b) 615 nm throughout the volatile matter burnout.

https://dx.doi.org/10.1021/acs.energyfuels.0c03921
Energy Fuels 2021, 35, 2313−2325

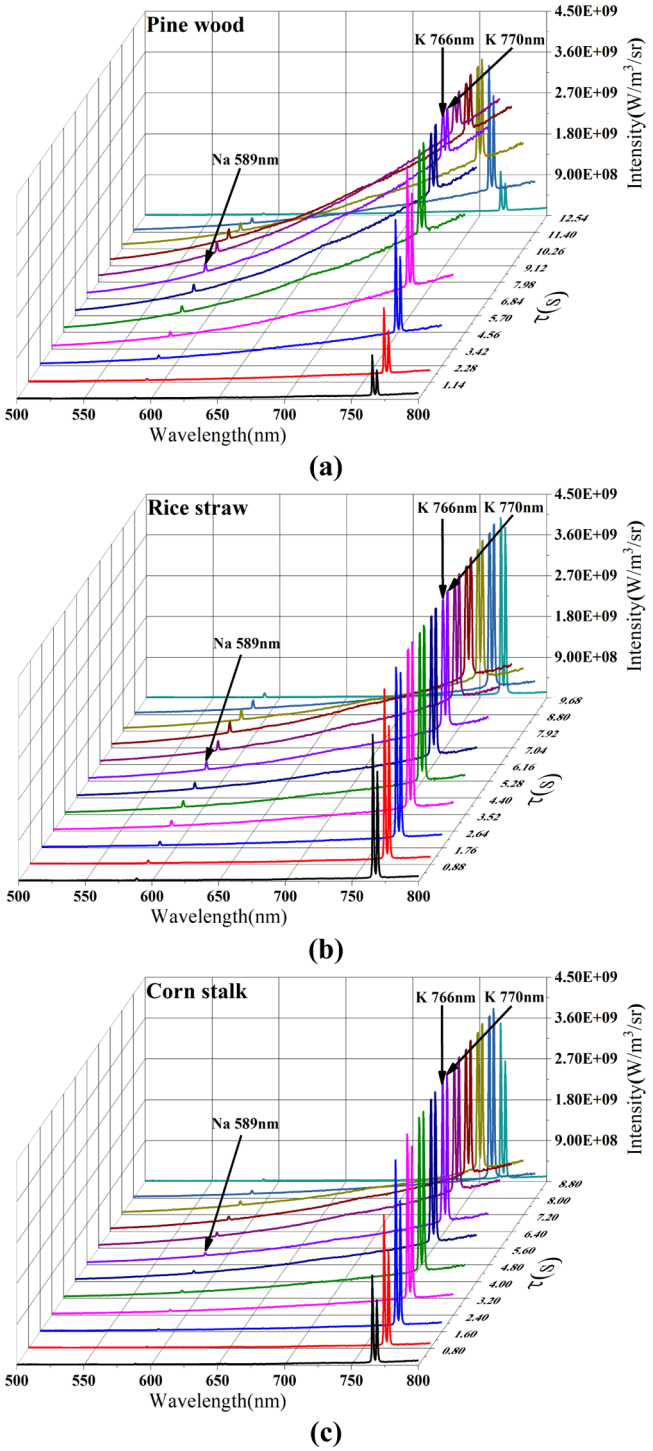

Figure 7. Radiation spectral distributions of flames of three different types of biomass (500−800 nm): (a) pine wood; (b) rice straw; and (c) corn stalk throughout the volatile burnout duration.

that the emissivity ratios are always less than unity during the combustion of the volatile flames of those three types of biomass. As the biomass pellets were heated and their temperature increased, the released amount of the volatile matter increased gradually, and the amount of generated soot increased accordingly. Upon ignition of the volatiles, the flame slowly approached the graybody behavior as the two wavelengths in this study were closely spaced (98 nm); as a result, the emissivity ratio gradually approached unity. By comparing Figures 8, 4, and 6, it can be concluded that the peaks of the emissivity ratios of the three different types of biomass all occurred

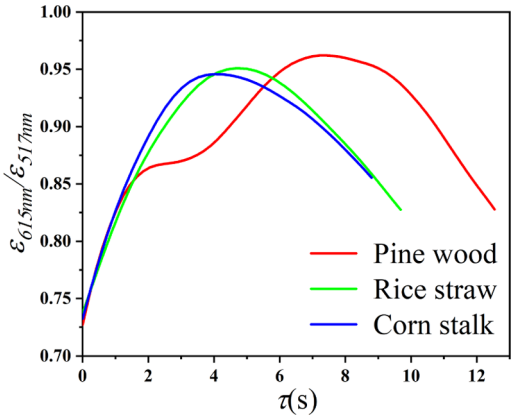

Figure 8. Emissivity ratios ($\varepsilon_{615\ nm}/\varepsilon_{517\ nm}$) of the biomass volatile matter flames as functions of their burnout.

at the moment when the flame size and radiation intensity were at their maximum, and they are approximately equal to 0.95. After the emissivity ratios reached their peak, with the gradual consumption of volatiles, the flame heights and radiation intensities gradually subsided, and the emissivity ratios also became gradually smaller. Therefore, whereas the volatile mater flames of biomass pellets do not behave as graybodies during the entire combustion process, they were found to approach such a behavior at their peak combustion moment. As a result of this behavior, the graybody assumption can cause errors in the temperature measurement of these transient flames. Therefore, accounting for the ratio of emissivity in image temperature measurements improves the accuracy of the measurement. The emissivity measurement can be provided from simultaneous spectrometric measurements.

After substituting the measured emissivity ratio into eq 3 and combining with the flame radiation intensity data measured by the camera (Figure 6), the corresponding two-dimensional flame temperature can be calculated, as shown in Figure 9. Substituting the calculated flame temperature into eq 4, the two-dimensional soot volume fraction can also be calculated, as shown in Figure 10.

It can be seen from Figure 9 that the high-temperature areas always appear on the right side of the middle and lower parts near the flame edge. This is because the thermocouple wires inside the pellets extend to the left under the pellets to provide support, and as a result, the flow field on the left side suffered a slight disturbance. The maximum recorded flame temperatures of pine wood, rice straw, and corn stalk were 1874 (at 6.84 s), 1878 (at 5.28 s), and 1878 K (at 7.2 s), respectively, which are remarkably similar. It can be seen from Figure 10 that the soot volume fraction of the flames gradually increased from the bottom along the flame height direction and then gradually decreased after reaching the peak in the middle and upper parts. The peak soot volume fractions of pine wood, rice straw, and corn stalk are 1.21 (at 6.84 s), 1.19 (at 6.16 s), and 1.16 ppm (at 4.8 s), respectively, which again are similar. According to the proximate analysis results in Table 1, it can be seen that the higher the volatile content of biomass pellets, the higher the soot volume fraction generated during combustion. The volatile content of pine wood pellet is higher than those of the other two biomass fuels. As a result, the size of the flame and the soot volume fraction in pinewood are somewhat larger, which make the radiant heat loss to be somewhat larger and results in a slightly lower maximum flame temperature. High temperatures promote fuel pyrolysis, which generates more soot precursors.[54] High temperatures can also increase the soot surface growth rate.[55] On the other hand, high temperatures promote soot oxidation, thereby reducing the amount of soot in the flame. The final soot generation is the result of competition between early nucleation, surface growth, and oxidation.

In order to verify the accuracy of the temperature measurement results by the image method, the S-type platinum−rhodium filament

https://dx.doi.org/10.1021/acs.energyfuels.0c03921
Energy Fuels 2021, 35, 2313−2325

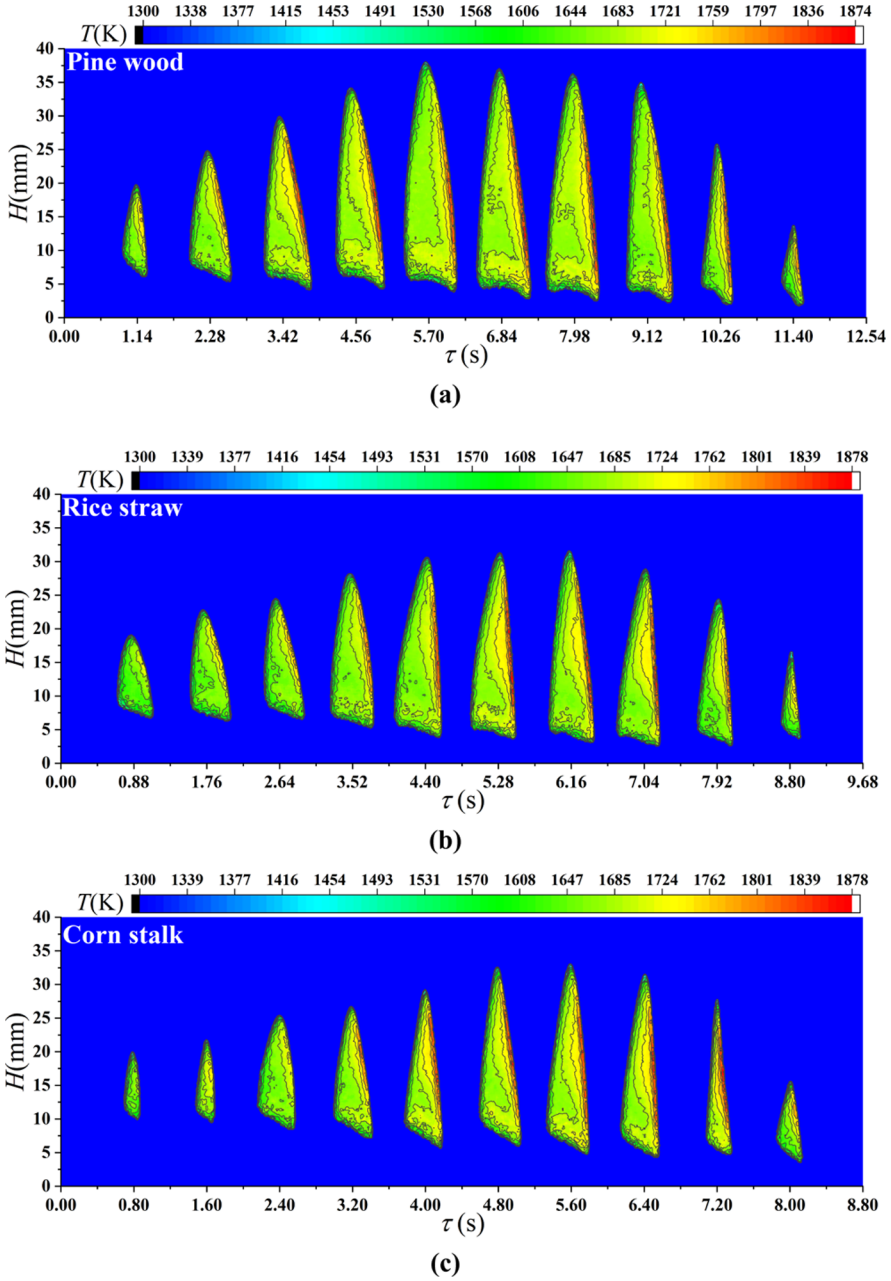

Figure 9. Temperature distributions in volatile matter flames: (a) pine wood; (b) rice straw; and (c) corn stalk throughout their burnout duration.

thermocouple was used for temperature measurement verification. It should be noted that the thermocouple temperature measurement was performed separately from spectral data and image data collection, so there was no mutual interference. The thermocouples used in the experiment had a diameter of 0.1 mm and a junction of 0.2 mm in diameter. During the experiment, the thermocouple was installed at the flame axis at a height of 20 mm directly above the upper surface of the pellets using a fixture. The thermocouple temperature measurement was corrected by cold junction and radiation. The comparison of the temperature measurements between the image method and the thermocouple reading is shown in Figure 11. The results measured by the two methods have a good consistency, and the maximum relative error of the image method is 2.7%.

The sampling frequency of the camera was set to 50 Hz during the experiments, but only 10 typical flame images are shown in Figure 4. Based on all flame images collected by the camera, the flame height change of the entire combustion stage was calculated. Results are shown in Figure 12, where the starting point of the flame height measurement is the upper surface of the biomass pellets (the bottom of the image is shown in Figure 4). It can be seen that during the combustion of all three types of biomass pellets, the heights of the flames first increased and then decreased. The maximum flame heights of pine wood, rice straw, and corn stalk were 37.5, 30.6, and 33.0 mm, respectively. The volatile content of the pine wood pellet was the highest, and its flame was also the tallest. The volatile contents of rice straw and corn stalk were similar, and the heights of their flames were nearly equivalent. Superimposed in Figure 12 are also the profiles of the average temperatures of the flames, which appear analogous to the corresponding flame height profiles. In each case, the average flame temperature was the highest when the flame height was the highest. During combustion, the peak average flame temperatures of pine wood, rice straw, and corn stalks were 1687, 1688, and 1691 K, respectively, which are remarkably close to each other.

https://dx.doi.org/10.1021/acs.energyfuels.0c03921
Energy Fuels 2021, 35, 2313−2325

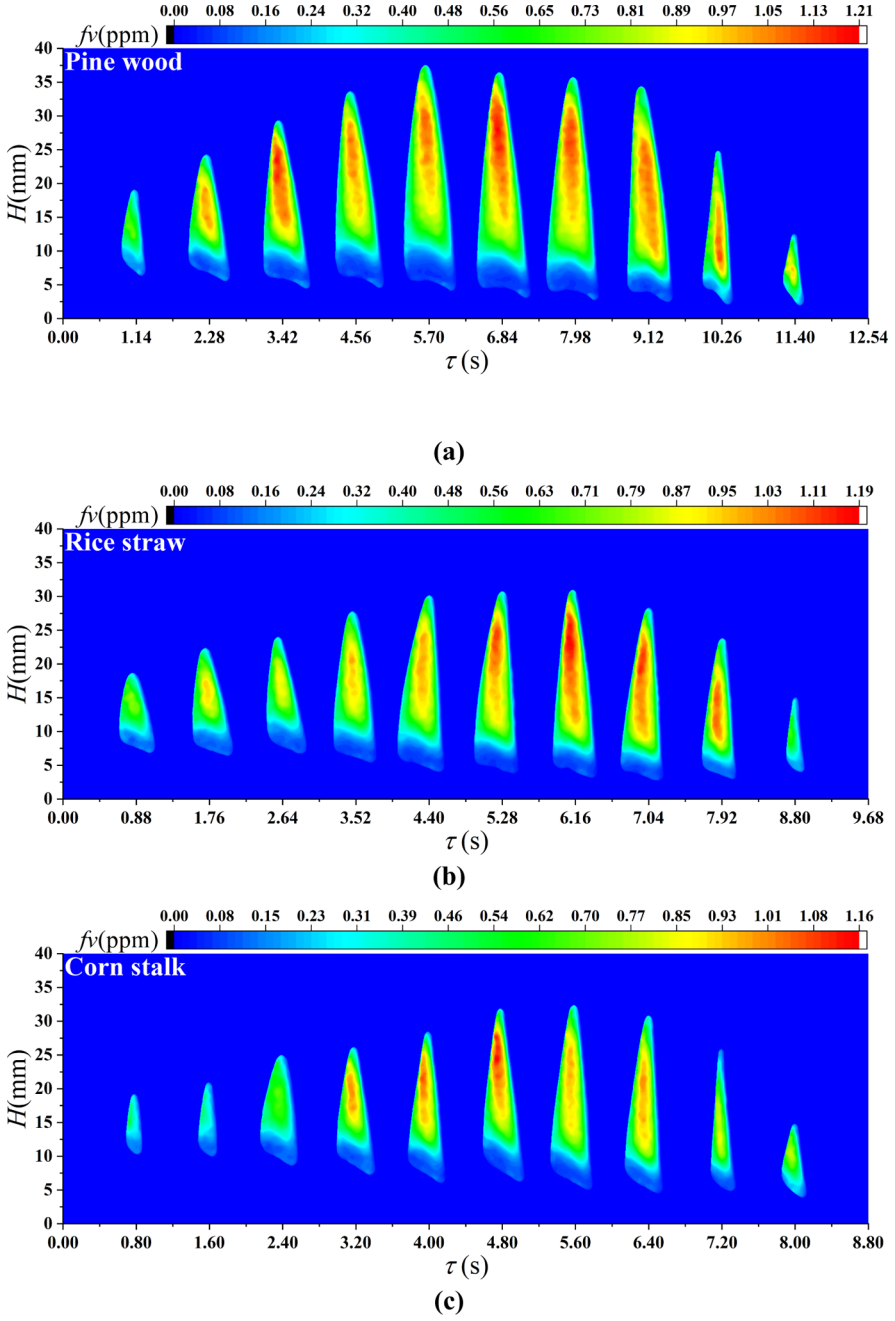

Figure 10. Soot volume fraction distributions in volatile matter flames of (a) pine wood; (b) rice straw; and (c) corn stalk throughout the volatile matter burnout.

Figure 13 shows that the profiles of the flame height have been superimposed to those of the average soot volume fractions throughout burnout. Again, the profiles of the average soot volume fractions of the flames appear to be analogous to the corresponding flame height profiles. Approximately, at the instant when the flame was the tallest, the average soot volume fraction was the largest, as the pyrolyzate fluxes of the devolatilizing biomass pellets are the most intense. The peak average soot volume fractions of pine wood, rice straw, and corn stalk flames were 0.61, 0.57, and 0.49 ppm, respectively. The peak average soot volume fraction generated by the combustion of pine wood pellet was the highest, and the peak average soot volume fraction generated by the rice straw pellet was the lowest. It can be concluded by comparing Figures 12 and 13 that the time when the flames reached their highest temperatures, their highest soot volume fractions nearly coincided and that both the maximum flame temperature and the highest soot concentration are positively correlated with the flame height.

The total amount of soot in Figure 14 was calculated from the results of Figure 10. First, the soot concentration in Figure 10 is the average value in the line of sight, and the flame is nearly axisymmetric. Therefore, the flame thickness at any pixel in the flame image can be determined by the flame diameter at the height of the pixel and the distance from the pixel to the flame axis. Then by multiplying the actual length and width corresponding to the pixel by the flame thickness corresponding to the pixel, the flame volume at the pixel is calculated. The total amount of soot in each pixel in the flame is obtained by multiplying the flame volume corresponding to each pixel by the average soot concentration in the line of sight. Finally, the total amount of soot in each pixel is summed to obtain the total amount of soot in the flame at each instant of time and is shown in Figure 14. In addition, Figure 14

https://dx.doi.org/10.1021/acs.energyfuels.0c03921
Energy Fuels 2021, 35, 2313−2325

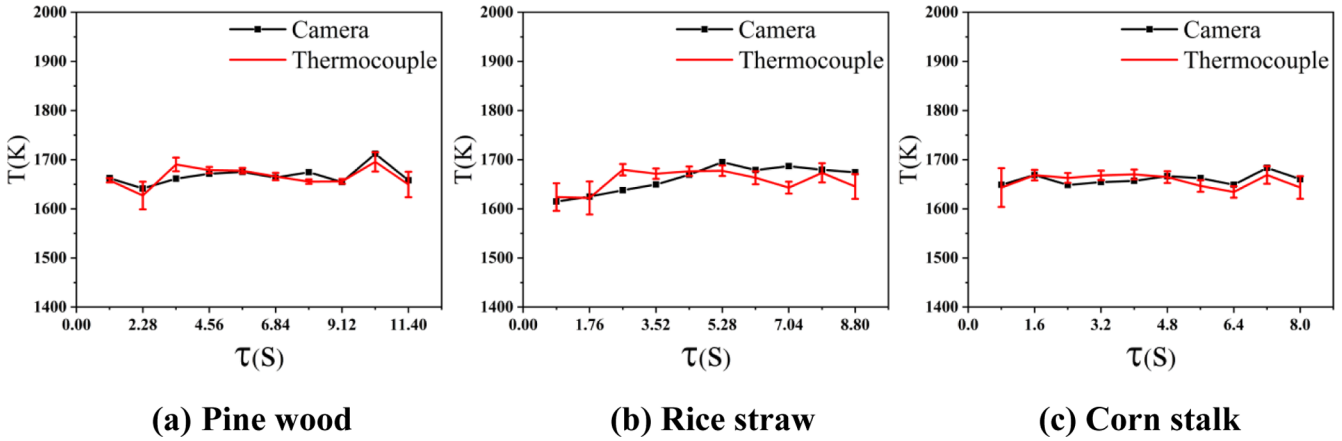

Figure 11. Comparison between average temperature measurements in the line of sight based on the camera and the measurements based on the thermocouple (at the flame axis, H = 20 mm).

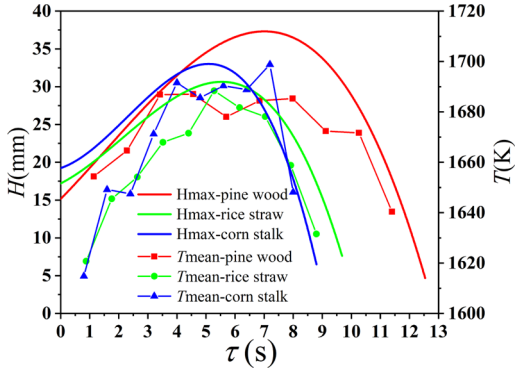

Figure 12. Flame height and average temperature profiles throughout burnout of the volatile matter of biomass pellets.

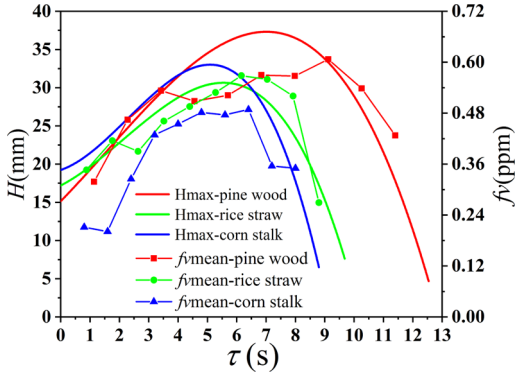

Figure 13. Flame height and average soot concentration profiles throughout burnout of the volatile matter of biomass pellets.

also shows the internal temperature of the biomass pellets, as measured by a platinum−rhodium filament thermocouple embedded in the center of each pellet. It can be seen that the internal temperature of the pellets gradually increased with time after they ignited. The heating ambient temperature of those pellets was approximately 1300 K (±20 K) in these experiments. Upon ignition of the volatile matter and formation of a flame, the temperature inside the pellets climbed to the neighborhood of 420 K. The internal temperature of the corn stalk pellet was a bit higher than the internal temperatures of the pine wood and rice straw pellets, which were similar to each other. The maximum amounts of soot in the volatile flames of pine wood, rice straw, and corn stalk were 0.68, 0.50, and 0.35 nL, respectively. For the three types of biomass

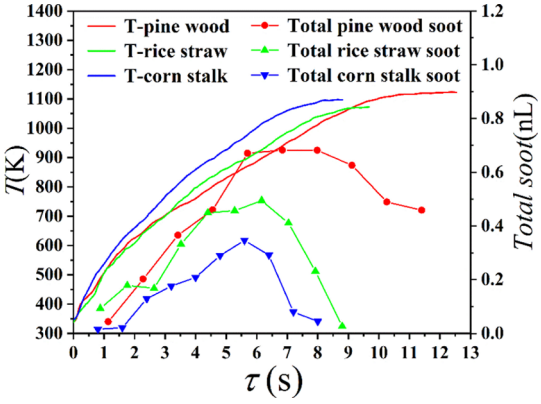

Figure 14. Comparison of the profiles of the internal temperature of pellets and the total amount of soot in the volatile matter flames of biomass pellets.

pellets considered herein, the total amounts of soot generated increased slowly at first and then decreased sharply after reaching peak values. The amount of soot generated during the entire combustion stage of the volatile matter was evaluated from the area under each curve of total soot generation. The pine wood pellets produced the largest amount of soot, followed by rice straw and then by corn straw. This trend is related to the volatile content of the raw materials, as shown in Table 1.

5. CONCLUSIONS

This investigation measured the temperature and soot volume fraction of volatile matter flames generated during the combustion of three types of biomass pellets. Both parameters were measured in real time based on the radiation spectra of the flames and their images in the visible light band. In these experiments, a camera equipped with a dual band-pass filter, with center wavelengths of 517 and 615 nm, was used to collect monochromatic radiation images. Such wavelengths were selected to avoid the interference of the characteristic lines of K (at 766.0 and 770.1 nm) and Na (at 589.0 nm) alkali metals. First, a spectrometer was used to collect the radiation spectra of the flames in the 500−800 nm wavelength band. Second, combined with a spectral emissivity model based on the polynomial fitting, the emissivity ratio was calculated at the response wavelengths of the filters. Finally, the measured emissivity ratio was used in the temperature measurement of the image method, and two-

https://dx.doi.org/10.1021/acs.energyfuels.0c03921
Energy Fuels 2021, 35, 2313−2325

dimensional temperature and soot volume fraction distributions of the flame were obtained. The following conclusions were drawn:

(1) The image temperature measurement method combined with the spectral analysis has relatively high measurement accuracy. Compared with a thermocouple reading, the maximum relative error is 2.7%.

(2) The flames of the pine wood, rice straw, and corn stalk pellets are not gray at all stages, but at the stage of intense combustion, the flames were nearly gray.

(3) The burnout times of the volatile flames of pine wood, rice straw, and corn stalk pellets were 12.54, 9.68, and 8.80 s, respectively, and the peak soot volume fractions were 1.21, 1.19, and 1.16 ppm, respectively. Both the duration of the flames and their peak soot volume fractions are positively correlated with the volatile content of biomass types.

(4) The soot volume fraction of the flames gradually increased from the bottom along the flame height direction and then gradually decreased after reaching the peak in the middle to the upper section of the flame.

(5) Finally, it is notable that the maximum flame temperatures in the volatile matter flames from biomass of different types (pine wood, rice husk, and corn stalk) and origins (woody and herbaceous) were remarkably similar (1874, 1878, and 1878 K).

AUTHOR INFORMATION

Corresponding Authors

Weijie Yan − *School of Electrical and Power Engineering, China University of Mining and Technology, Xuzhou 221116, China;* orcid.org/0000-0002-3912-6028; Phone: +86 516 8359-2000; Email: yanweijie@cumt.edu.cn

Yiannis A. Levendis − *Mechanical and Industrial Engineering Department, Northeastern University, Boston, Massachusetts 02115, United States;* orcid.org/0000-0002-8158-2123; Phone: +1 617 373-3806; Email: y.levendis@northeastern.edu

Authors

Kuangyu Li − *School of Electrical and Power Engineering, China University of Mining and Technology, Xuzhou 221116, China*

Tianze Yu − *School of Electrical and Power Engineering, China University of Mining and Technology, Xuzhou 221116, China*

Xianliang Huang − *School of Electrical and Power Engineering, China University of Mining and Technology, Xuzhou 221116, China*

Lingbo Yu − *School of Electrical and Power Engineering, China University of Mining and Technology, Xuzhou 221116, China*

Aidin Panahi − *Mechanical and Industrial Engineering Department, Northeastern University, Boston, Massachusetts 02115, United States*

Complete contact information is available at: https://pubs.acs.org/10.1021/acs.energyfuels.0c03921

Author Contributions

W.Y.: analysis principle and explanation of results. K.L.: experiments and data processing. T.Y.: experiments and data processing. X.H.: blackbody calibration. L.Y.: thermocouple temperature measurement. A.P.: explanation of results. Y.A.L.: organizing the article.

Funding

The research was supported by the National Natural Science Foundation of China (no. 51706239), the China Postdoctoral Science Foundation Grant (no. 2019M661982), the Foundation of the State Key Laboratory of Coal Combustion (FSKLCCA2006), and the Fundamental Research Funds for the Central Universities (nos. 2018QNA11 and 2019GF15). The involvement of coauthor YAL was supported by the US National Science Foundation under Grant # 1810961.

Notes

The authors declare no competing financial interest.

REFERENCES

(1) Jenkins, B. M.; Baxter, L. L.; Miles, T. R. Combustion properties of biomass. *Fuel Process. Technol.* **1998**, *54*, 17−46.

(2) Al-Omari, S.-A. B.; Kawajiri, K.; Yonesawa, T. Soot processes in a methane-fueled furnace and their impact on radiation heat transfer to furnace walls. *Int. J. Heat Mass Tran.* **2001**, *44*, 2567−2581.

(3) Atiku, F. A.; Lea-Langton, A. R.; Bartle, K. D.; Jones, J. M.; Williams, A.; Burns, I.; Humphries, G. Some Aspects of the Mechanism of Formation of Smoke from the Combustion of Wood. *Energy Fuels* **2017**, *31*, 1935−1944.

(4) Josephson, A. J.; Linn, R. R.; Lignell, D. O. Modeling soot formation from solid complex fuels. *Combust. Flame* **2018**, *196*, 265−283.

(5) Fitzpatrick, E. M.; Jones, J. M.; Pourkashanian, M.; Ross, A. B.; Williams, A.; Bartle, K. D. Mechanistic Aspects of Soot Formation from the Combustion of Pine Wood. *Energy Fuels* **2008**, *22*, 3771−3778.

(6) Fitzpatrick, E. M.; Bartle, K. D.; Kubacki, M. L.; Jones, J. M.; Pourkashanian, M.; Ross, A. B.; Williams, A.; Kubica, K. The mechanism of the formation of soot and other pollutants during the co-firing of coal and pine wood in a fixed bed combustor. *Fuel* **2009**, *88*, 2409−2417.

(7) Wijayanta, A. T.; Saiful Alam, M.; Nakaso, K.; Fukai, J.; Shimizu, M. Optimized combustion of bio mass volatiles by varying O-2 and CO2 levels: A numerical simulation using a highly detailed soot formation reaction mechanism. *Bioresour. Technol.* **2012**, *110*, 645−651.

(8) Li, Y.; Tan, H.; Wang, X.; Bai, S.; Mei, J.; You, X.; Ruan, R.; Yang, F. Characteristics and Mechanism of Soot Formation during the Fast Pyrolysis of Biomass in an Entrained Flow Reactor. *Energy Fuels* **2018**, *32*, 11477−11488.

(9) Septien, S.; Valin, S.; Peyrot, M.; Dupont, C.; Salvador, S. Characterization of char and soot from millimetric wood particles pyrolysis in a drop tube reactor between 800 degrees C and 1400 degrees C. *Fuel* **2014**, *121*, 216−224.

(10) Trubetskaya, A.; Jensen, P. A.; Jensen, A. D.; Garcia Llamas, A. D.; Umeki, K.; Gardini, D.; Kling, J.; Bates, R. B.; Glarborg, P. Effects of several types of biomass fuels on the yield, nanostructure and reactivity of soot from fast pyrolysis at high temperatures. *Appl. Energy* **2016**, *171*, 468−482.

(11) Jin, Q.; Wang, X.; Li, S.; Mikulčić, H.; Bešenić, T.; Deng, S.; Vujanović, M.; Tan, H.; Kumfer, B. M. Synergistic effects during co-pyrolysis of biomass and plastic: Gas, tar, soot, char products and thermogravimetric study. *J. Energy Inst.* **2019**, *92*, 108−117.

(12) Li, Y.; Wang, X.; Tan, H.; Bai, S.; Mikulčić, H.; Yang, F. Evolution of PM2.5 from biomass high-temperature pyrolysis in an entrained flow reactor. *J. Energy Inst.* **2019**, *92*, 1548−1556.

(13) Wiinikka, H.; Gebart, R.; Boman, C.; Boström, D.; Nordin, A.; Öhman, M. High-temperature aerosol formation in wood pellets flames: Spatially resolved measurements. *Combust. Flame* **2006**, *147*, 278−293.
(14) Nyström, R.; Lindgren, R.; Avagyan, R.; Westerholm, R.; Lundstedt, S.; Boman, C. Influence of Wood Species and Burning Conditions on Particle Emission Characteristics in a Residential Wood Stove. *Energy Fuels* **2017**, *31*, 5514−5524.
(15) Yousaf, B.; Liu, G.; Abbas, Q.; Wang, R.; Ubaid Ali, M.; Ullah, H.; Liu, R.; Zhou, C. Systematic investigation on combustion characteristics and emission-reduction mechanism of potentially toxic elements in biomass- and biochar-coal co-combustion systems. *Appl. Energy* **2017**, *208*, 142−157.
(16) Colom-Díaz, J. M.; Alzueta, M. U.; Fernandes, U.; Costa, M. Emissions of polycyclic aromatic hydrocarbons from a domestic pellets-fired boiler. *Fuel* **2019**, *247*, 108−112.
(17) Mustafa, B. G.; Kiah, M. H. M.; Irshad, A.; Andrews, G. E.; Phylaktou, H. N.; Li, H.; Gibbs, B. M. Rich biomass combustion: Gaseous and particle number emissions. *Fuel* **2019**, *248*, 221−231.
(18) Baeza-Romero, M. T.; Wilson, J. M.; Fitzpatrick, E. M.; Jones, J. M.; Williams, A. In Situ Study of Soot from the Combustion of a Biomass Pyrolysis Intermediate-Eugenol-and n-Decane Using Aerosol Time of Flight Mass Spectrometry. *Energy Fuels* **2010**, *24*, 439−445.
(19) Wilson, J. M.; Baeza-Romero, M. T.; Jones, J. M.; Pourkashanian, M.; Williams, A.; Lea-Langton, A. R.; Ross, A. B.; Bartle, K. D. Soot Formation from the Combustion of Biomass Pyrolysis Products and a Hydrocarbon Fuel, n-Decane: An Aerosol Time Of Flight Mass Spectrometer (ATOFMS) Study. *Energy Fuels* **2013**, *27*, 1668−1678.
(20) Lea-Langton, A. R.; Baeza-Romero, M. T.; Boman, G. V.; Brooks, B.; Wilson, A. J. M.; Atika, F.; Bartle, K. D.; Jones, J. M.; Williams, A. A study of smoke formation from wood combustion. *Fuel Process. Technol.* **2015**, *137*, 327−332.
(21) Bierkandt, T.; Hemberger, P.; Osswald, P.; Krüger, D.; Köhler, M.; Kasper, T. Flame structure of laminar premixed anisole flames investigated by photoionization mass spectrometry and photoelectron spectroscopy. *Proc. Combust. Inst.* **2019**, *37*, 1579−1587.
(22) Storch, M.; Koegl, M.; Altenhoff, M.; Will, S.; Zigan, L. Investigation of soot formation of spark-ignited ethanol-blended gasoline sprays with single- and multi-component base fuels. *Appl. Energy* **2016**, *181*, 278−287.
(23) Gao, Z.; Zhu, L.; Zou, X.; Liu, C.; Tian, B.; Huang, Z. Soot reduction effects of dibutyl ether (DBE) addition to a biodiesel surrogate in laminar coflow diffusion flames. *Proc. Combust. Inst.* **2019**, *37*, 1265−1272.
(24) Tóth, P.; Brackmann, C.; Ögren, Y.; Mannazhi, M. N.; Simonsson, J.; Sepman, A.; Bengtsson, P.-E.; Wiinikka, H. Experimental and numerical study of biomass fast pyrolysis oil spray combustion: Advanced laser diagnostics and emission spectrometry. *Fuel* **2019**, *252*, 125−134.
(25) Merchan-Merchan, W.; McCollam, S.; Pugliese, J. F. C. Soot formation in diffusion oxygen-enhanced biodiesel flames. *Fuel* **2015**, *156*, 129−141.
(26) Göktepe, B.; Umeki, K.; Gebart, R. Does distance among biomass particles affect soot formation in an entrained flow gasification process. *Fuel Process. Technol.* **2016**, *141*, 99−105.
(27) Göktepe, B.; Umeki, K.; Hazim, A.; Lundström, T. S.; Gebart, R. Soot reduction in an entrained flow gasifier of biomass by active dispersion of fuel particles. *Fuel* **2017**, *201*, 111−117.
(28) Sepman, A.; Ögren, Y.; Qu, Z.; Wiinikka, H.; Schmidt, F. M. Real-time in situ multi-parameter TDLAS sensing in the reactor core of an entrained-flow biomass gasifier. *Proc. Combust. Inst.* **2017**, *36*, 4541−4548.
(29) Sepman, A.; Ögren, Y.; Qu, Z.; Wiinikka, H.; Schmidt, F. M. Tunable Diode Laser Absorption Spectroscopy Diagnostics of Potassium, Carbon Monoxide, and Soot in Oxygen-Enriched Biomass Combustion Close to Stoichiometry. *Energy Fuels* **2019**, *33*, 11795−11803.
(30) Tóth, P.; Ögren, Y.; Sepman, A.; Vikström, T.; Gren, P.; Wiinikka, H. Spray combustion of biomass fast pyrolysis oil: Experiments and modeling. *Fuel* **2019**, *237*, 580−591.
(31) Draper, T. S.; Zeltner, D.; Tree, D. R.; Xue, Y.; Tsiava, R. Two-dimensional flame temperature and emissivity measurements of pulverized oxy-coal flames. *Appl. Energy* **2012**, *95*, 38−44.
(32) Jing, W.; Wu, Z.; Zhang, W.; Fang, T. Measurements of soot temperature and KL factor for spray combustion of biomass derived renewable fuels. *Energy* **2015**, *91*, 758−771.
(33) Levendis, Y. A.; Joshi, K.; Khatami, R.; Sarofim, A. F. Combustion behavior in air of single particles from three different coal ranks and from sugarcane bagasse. *Combust. Flame* **2011**, *158*, 452−465.
(34) Khatami, R.; Levendis, Y. A. On the deduction of single coal particle combustion temperature from three-color optical pyrometry. *Combust. Flame* **2011**, *158*, 1822−1836.
(35) Araujo, A. Multi-spectral pyrometry-a review. *Meas. Sci. Technol.* **2017**, *28*, 082002.
(36) Fu, T.; Duan, M.; Tang, J.; Shi, C. Measurements of the directional spectral emissivity based on a radiation heating source with alternating spectral distributions. *Int. J. Heat Mass Tran.* **2015**, *90*, 1207−1213.
(37) Zheng, S.; Yang, Y.; Li, X.; Liu, H.; Yan, W.; Sui, R.; Lu, Q. Temperature and emissivity measurements from combustion of pine wood, rice husk and fir wood using flame emission spectrum. *Fuel Process. Technol.* **2020**, *204*, 106423.
(38) Yan, W.; Li, K.; Huang, X.; Yu, L.; Lou, C.; Chen, Y. Online Measurement of the Flame Temperature and Emissivity during Biomass Volatile Combustion Using Spectral Thermometry and Image Thermometry. *Energy Fuels* **2020**, *34*, 907−919.
(39) Liu, H. W.; Zheng, S.; Zhou, H. C.; Qi, C. B. Measurement of distributions of temperature and wavelength-dependent emissivity of a laminar diffusion flame using hyper-spectral imaging technique. *Meas. Sci. Technol.* **2016**, *27*, 025201.
(40) Sun, Y.; Lou, C.; Zhou, H. A simple judgment method of gray property of flames based on spectral analysis and the two-color method for measurements of temperatures and emissivity. *Proc. Combust. Inst.* **2011**, *33*, 735−741.
(41) Shao, L.; Zhou, Z.; Chen, L.; Guo, L.; Chen, B.; Liang, L. Study of an improved two-colour method integrated with the emissivity ratio model and its application to air- and oxy-fuel flames in industrial furnaces. *Measurement* **2018**, *123*, 54−61.
(42) Xu, Y.; Li, S.; Yuan, Y.; Yao, Q. Measurement on the Surface Temperature of Dispersed Chars in a Flat-Flame Burner Using Modified RGB Pyrometry. *Energy Fuels* **2017**, *31*, 2228−2235.
(43) Yan, W.; Panahi, A.; Levendis, Y. A. Spectral emissivity and temperature of heated surfaces based on spectrometry and digital thermal imaging - Validation with thermocouple temperature measurements. *Exp. Therm. Fluid Sci.*. **2020**, *112*. DOI: 10.1016/j.expthermflusci.2019.110017
(44) Yan, W.; Zheng, S.; Zhou, H. Experiments investigation on 2D distribution of soot temperature and volume fraction by image processing of visible radiation. *Appl. Therm. Eng.* **2017**, *124*, 1014−1022.
(45) Cignoli, F.; De Iuliis, S.; Manta, V.; Zizak, G. Two dimensional two-wavelength emission technique for soot diagnostics. *Appl. Opt.* **2001**, *40*, 5370−5378.
(46) Kuhn, P. B.; Ma, B.; Connelly, B. C.; Smooke, M. D.; Long, M. B. Soot and thin-filament pyrometry using a color digital camera. *Proc. Combust. Inst.* **2011**, *33*, 743−750.
(47) Krishnan, S. S.; Lin, K.-C.; Faeth, G. M. Optical properties in the visible of overfire soot in large buoyant turbulent diffusion flames. *J. Heat Tran.* **2000**, *122*, 517−524.
(48) Li, K.; Yan, W.; Huang, X.; Yu, L.; Chen, Y.; Lou, C. In-situ measurement of temperature and potassium concentration during the combustion of biomass pellets based on the emission spectrum. *Fuel* **2021**, *289*, 119863.

(49) Wang, X.; Bai, S.; Jin, Q.; Li, S.; Li, Y.; Li, Y.; Tan, H. Soot formation during biomass pyrolysis: Effects of temperature, water-leaching, and gas-phase residence time. *J. Anal. Appl. Pyrolysis* **2018**, *134*, 484−494.
(50) Liu, H.; Zheng, S.; Wang, T. Experimental study of radiation characteristics and temperature distributions of gasoline and biomass flame. *IET Renew. Power Gener.* **2019**, *13*, 1833−1839.
(51) Wen, C.-D. Investigation of steel emissivity behaviors: Examination of Multispectral Radiation Thermometry (MRT) emissivity models. *Int. J. Heat Mass Transfer* **2010**, *53*, 2035−2043.
(52) Seeger, T. S.; Machado, E. Q.; Flores, E. M. M.; Mello, P. A.; Duarte, F. A. Direct sampling graphite furnace atomic absorption spectrometry - feasibility of Na and K determination in desalted crude oil. *Spectrochim. Acta Part B At. Spectrosc.* **2018**, *141*, 28−33.
(53) He, X.; Lou, C.; Qiao, Y.; Lim, M. In-situ measurement of temperature and alkali metal concentration in municipal solid waste incinerators using flame emission spectroscopy. *Waste Manag.* **2020**, *102*, 486−491.
(54) Zhang, J.; Megaridis, C. M. Soot microstructure in steady and flickering laminar methane/air diffusion flames. *Combust. Flame* **1998**, *112*, 473−484.
(55) Barlow, R. S.; Frank, J. H. Effects of turbulence on species mass fractions in methane/air jet flames. *Symp. Combust. Proc.* **1998**, *27*, 1087−1095.

https://dx.doi.org/10.1021/acs.energyfuels.0c03921
Energy Fuels 2021, 35, 2313−2325